The Astrophysical Journal Letters, 949:L7 (11pp), 2023 May 20 https://doi.org/10.3847/2041-8213/acd1eb


# Properties of the Extremely Energetic GRB 221009A from Konus-WIND and SRG/ART-XC Observations

D. Frederiks[1], D. Svinkin[1], A. L. Lysenko[1], S. Molkov[2], A. Tsvetkova[1], M. Ulanov[1], A. Ridnaia[1], A. A. Lutovinov[2], I. Lapshov[2], A. Tkachenko[2], and V. Levin[2]
[1] Ioffe Institute, 26 Politekhnicheskaya, St Petersburg, 194021, Russia; fred@mail.ioffe.ru, ddfrederiks@gmail.com
[2] Space Research Institute, Russian Academy of Sciences, Profsoyuznaya 84/32, 117997 Moscow, Russia
*Received 2023 February 26; revised 2023 April 30; accepted 2023 May 2; published 2023 May 18*

## Abstract

We report on Konus-WIND (KW) and Mikhail Pavlinsky Astronomical Roentgen Telescope – X-ray Concentrator (ART-XC) observations and analysis of a nearby GRB 221009A, the brightest $\gamma$-ray burst (GRB) detected by KW for >28 yr of observations. The prompt, pulsed phase of the burst emission lasts for ~600 s and is followed by a steady power-law decay lasting for more than 25 ks. From the analysis of the KW and ART-XC light curves and the KW spectral data, we derive time-averaged spectral peak energy of the burst $E_p \approx 2.6$ MeV, $E_p$ at the brightest emission peak $\approx 3.0$ MeV, the total 20 keV–10 MeV energy fluence of $\approx 0.22$ erg cm$^{-2}$, and the peak energy flux in the same band of $\approx 0.031$ erg cm$^{-2}$ s$^{-1}$. The enormous observed fluence and peak flux imply, at redshift $z = 0.151$, huge values of isotropic energy release $E_{\rm iso} \approx 1.2 \times 10^{55}$ erg (or $\gtrsim 6.5$ solar rest mass) and isotropic peak luminosity $L_{\rm iso} \approx 3.4 \times 10^{54}$ erg s$^{-1}$ (64 ms scale), making GRB 221009A the most energetic and one of the most luminous bursts observed since the beginning of the GRB cosmological era in 1997. The isotropic energetics of the burst fit nicely both "Amati" and "Yonetoku" hardness–intensity correlations for >300 KW long GRBs, implying that GRB 221009A is most likely a very hard, super-energetic version of a "normal" long GRB.

*Unified Astronomy Thesaurus concepts:* Gamma-ray bursts (629)

## 1. Introduction

Cosmological gamma-ray bursts (GRBs) are thought to be produced by at least two distinct classes of catastrophic events: mergers of binary compact objects, such as two neutron stars or a neutron star and a black hole, typically produce short, $\lesssim 2$ s, so-called type I GRBs; the core collapse of massive stars produce typically long (type II) GRBs. See, e.g., Zhang et al. (2009) for more information on the type I/II classification scheme.

GRBs have been the target of many observational efforts at all wavelengths, from a multitude of space- and ground-based observatories (see Tsvetkova et al. 2022 for a recent GRB facility review). GRBs occur at a rate of about 1 day$^{-1}$ and, with many thousand events observed to date (Mazets et al. 1981; Briggs et al. 1996; Atteia et al. 1999; Frontera et al. 2009; Guidorzi et al. 2011; Goldstein et al. 2013; Lien et al. 2016; Svinkin et al. 2016; Kozlova et al. 2019), the basic properties of their prompt $\gamma$-ray emissions are well established. The bursts last from a fraction of a second to several thousand seconds, showing a wide range of structures in their light curves and having a typical peak energy in the 100 keV–1 MeV range. The overall observed GRB fluences range from $10^{-7}$ to as high as $10^{-3}$ erg cm$^{-2}$.

The GRB cosmological origin was established about 25 yr ago, and it became clear that the observed flux corresponds to an enormous emitted energy, making GRBs the most luminous objects in the sky. The measured GRB isotropic-equivalent energy release $E_{\rm iso}$ and isotropic peak luminosity $L_{\rm iso}$ have broad distributions (Amati et al. 2002, 2008; Yonetoku et al. 2004; Gruber et al. 2011; Atteia et al. 2017; Tsvetkova et al. 2017, 2021) and tend to follow a number of empirical correlations between rest-frame parameters of GRB prompt emission, e.g., the "Amati" (Amati et al. 2002), "Yonetoku" (Yonetoku et al. 2004) and "Ghirlanda" (Ghirlanda et al. 2007) relations. The most intense GRBs reaching close to $E_{\rm iso} \sim 10^{55}$ erg (Abdo et al. 2009; Greiner et al. 2009; Tsvetkova et al. 2017) and $L_{\rm iso} \sim 5 \times 10^{54}$ erg s$^{-1}$ (Frederiks et al. 2013; Svinkin et al. 2021). An upper limit on GRB isotropic energy has recently been predicted ($E_{\rm iso} \sim 3.8 \times 10^{54}$ erg; Dado & Dar 2022), which, together with a strong cutoff of the $E_{\rm iso}$ distribution above $1–3 \times 10^{54}$ erg, suggested from the analysis of Konus-WIND (KW) and Fermi Gamma-ray Burst Monitor (GBM) samples of GRBs with known redshifts (Atteia et al. 2017; Tsvetkova et al. 2017, 2021), imply very rare detections of extremely energetic GRBs. Bright, nearby GRBs provide a unique opportunity to probe the central-engine physics, prompt emission, and afterglow emission mechanisms, as well as the GRB local environment. So far, only a few such bursts have been observed.

On 2022 October 9 at about 13:17:00 UTC, an extremely intense GRB 221009A was detected by many space-based missions: Fermi (GBM and Large Area Telescope; Bissaldi et al. 2022; Lesage et al. 2022; Pillera et al. 2022; Veres et al. 2022), KW (Frederiks et al. 2022; Svinkin et al. 2022), AGILE (MCAL and GRID; Piano et al. 2022; Ursi et al. 2022), INTEGRAL (SPI-ACS; Gotz et al. 2022), Insight-HXMT (Tan et al. 2022), Solar Orbiter (STIX; Xiao et al. 2022), Spektr-RG (Astronomical Roentgen Telescope – X-ray Concentrator, hereafter ART-XC; Lapshov et al. 2022), GRBAlpha (Ripa et al. 2022), SIRI-2 (Mitchell et al. 2022), GECAM-C (Liu et al. 2022), and BepiColombo (MGNS; Kozyrev et al. 2022). The initial analysis of the burst showed that the prompt emission was so intense that it saturated almost all instruments.

About 53 minutes later, the bright hard X-ray and optical afterglow, initially designated as a transient Swift J1913.1 +1946, was detected by the Neil Gehrels Swift Observatory (Burst Alert Telescope, BAT; X-Ray Telescope, XRT; and Ultraviolet/Optical Telescope, UVOT; Dichiara et al. 2022; Krimm et al. 2022). The multiwavelength follow-up observations led to the detection of bright optical afterglow and spectroscopic redshift determination of $z = 0.151$, which implies a luminosity distance $d_L$ of 745 Mpc (Castro-Tirado et al. 2022; de Ugarte Postigo et al. 2022a; Malesani et al. 2023).[3] The possible supernova associated with the burst was discovered a few days after the GRB (Belkin et al. 2022a, 2022b; de Ugarte Postigo et al. 2022b).

A preliminary analysis of the KW detection revealed that GRB 221009A is the most intense $\gamma$-ray burst observed by the instrument (Frederiks et al. 2022). The brightness of the main burst episode did not allow us to perform the standard KW spectral analysis of the emission. However, with preliminary dead-time (DT) corrections applied, a rough estimate of the energy fluence of the 600 s long burst was obtained ($\sim$0.052 erg cm$^{-2}$), which is the highest value observed for GRBs for 28 yr of the KW operation.

The Mikhail Pavlinsky ART-XC telescope observed GRB 221009A outside its field of view (FoV). The burst signal passed through the telescope's side shield, but it was clearly visible in all seven detectors. A preliminary analysis showed that the GRB light curve has a complex shape, which can be restored with good accuracy (Lapshov et al. 2022).

In this work, we present the detailed analysis of KW and ART-XC detections of GRB 221009A. Both instruments operate in interplanetary space, in orbits around Lagrange points L1 and L2, respectively, which allowed us observe the burst for its whole duration in stable background conditions. From the KW temporal and spectral data corrected for instrumental effects and the ART-XC light-curve data, we derive key parameters of GRB 221009A prompt emission in the observer frame, estimate the event energetics in the cosmological rest frame of the source, and discuss this extraordinary burst in the context of the KW sample of long GRBs.

Throughout the paper all errors reported are 90% conf. levels unless otherwise specified. We adopt the conventional notation $Q_k = Q/10^k$ and use cgs units unless otherwise noted.

## 2. Observations

### 2.1. Konus-Wind

GRB 221009A triggered KW at $T_0$(KW) = 47821.648 s UT (13:17:01.648) on 2022 October 22. The KW trigger time corresponds to the Earth-crossing time $T_0$=47820.401 s UT (13:17:00.401) that is $\sim$0.4 s after the GBM trigger and $\sim$3200 s before the BAT trigger on Swift J1913.1 + 1946. Throughout the paper, we report all times with respect to this reference point unless otherwise specified.

KW (Aptekar et al. 1995) consists of two cylindrical NaI(Tl) detectors, S1 and S2, mounted on the opposite sides of the rotationally stabilized Wind spacecraft. The burst triggered S2, with the incident angle of 48°.2 and an effective area of 90–150 cm$^2$, depending on the photon energy. S1 observed the burst through the spacecraft body and the rear structure of the detector, with the incident angle of 132°.8. The attenuation of the burst emission detected in S1 cannot be easily quantified, but unsaturated data from this detector can be used as a reference.

In the triggered detector S2, count rates were recorded by time history analyzers (THAs) in three energy bands: G1(20–80 keV), G2(80–320 keV), and G3(320–1220 keV). The record starts at $-0.512$ s, where 2 ms resolution light curves are available up to 0.512 s; at 16 ms, up to 33.280 s are available; at 64 ms, up to 98.816 s are available; and at 256 ms —up to 229.632 s are available. Starting from $T_0$, 64 multichannel energy spectra were measured by two pulse-height analyzers: PHA1 (63 channels, 20-1200 keV) and PHA2 (60 channels, 0.4–16.5 MeV). For spectra 1 to 56, the accumulation time varies between 64 ms and 8.192 s. For the last eight spectra, measured from 192.256 s to 257.792 s, the accumulation time is fixed at 8.192 s.

The KW "waiting mode THA" (hereafter BGA) data are available in G1, G2, and G3 from both detectors up to 251.371 s, along with the count rates at energies $\sim$16.5–22 MeV (the Z channel), all with a resolution of 2.944 s. In the interval from 251.371 s, when the measurements were stopped due to the data readout, to $\sim$5070 s, when the waiting mode resumed, only the count rates in G2 are available from S2, with the time resolution of 3.68 s and the very rough quantization of 256 counts per time bin (the "housekeeping THA", hereafter HGA, data).

The reduction of the light-curve and spectral data is made using standard KW analysis tools and procedures (described, e.g., in Svinkin et al. 2016; Tsvetkova et al. 2017, 2021; Lysenko et al. 2022). Standard KW DT corrections (Mazets et al. 1999b) are applied to the time history and spectral data outside the region of the most intense emission, from 216 to 270 s, where additional flux saturation and pulse-pileup corrections are required (see Appendix A for the details).

For the prompt emission light curves (up to 650 s), we assume a constant background estimated from a preburst interval from $-2500$ s to $-150$ s, during which count rates in all energy ranges of both KW detectors are consistent with being Poisson distributed. To analyze the burst's extended emission on timescales of tens of kiloseconds, we use linear background approximations, constructed, for each channel, from time-averaged count rates in two time intervals: 10 ks preceding $T_0$ and from 30 to 40 ks after the trigger. For G2 and G3, these approximations are consistent with the constant background we use for the prompt emission analysis; however, for G1, a slight negative slope is required (mainly due to the activity of bright Galactic X-ray sources).

Background spectra were extracted during a "quiet" time interval from 74 s to 123 s, and the detector energy scale was calibrated using the background spectra. The spectral analysis is performed with XSPEC (Arnaud 1996),[4] version 12.11.1, using the $\chi^2$ statistic and the Band GRB function (Band et al. 1993) if not mentioned otherwise: $f(E) \propto E^{\alpha}\exp(-(2+\alpha)E/E_{\rm peak})$ for $E < E_{\rm peak}(\alpha-\beta)/(2+\alpha)$, and $f(E) \propto E^{\beta}$ for $E \geqslant E_{\rm peak}(\alpha-\beta)/(2+\alpha)$, where $\alpha$ is the low-energy photon index, $E_{\rm p}$ is the peak energy in the $\nu F_\nu$ spectrum, and $\beta$ is the photon index at higher energies. The spectral model is normalized to the energy flux in the 20 keV–10 MeV range, a standard band for the KW GRB spectral analysis.

[3] Assuming a flat $\Lambda$CDM cosmology with $H_0 = 67.8$ km s$^{-1}$ Mpc$^{-1}$ $\Omega_M = 0.315$ (Planck Collaboration et al. 2020).

[4] https://heasarc.gsfc.nasa.gov/xanadu/xspec/

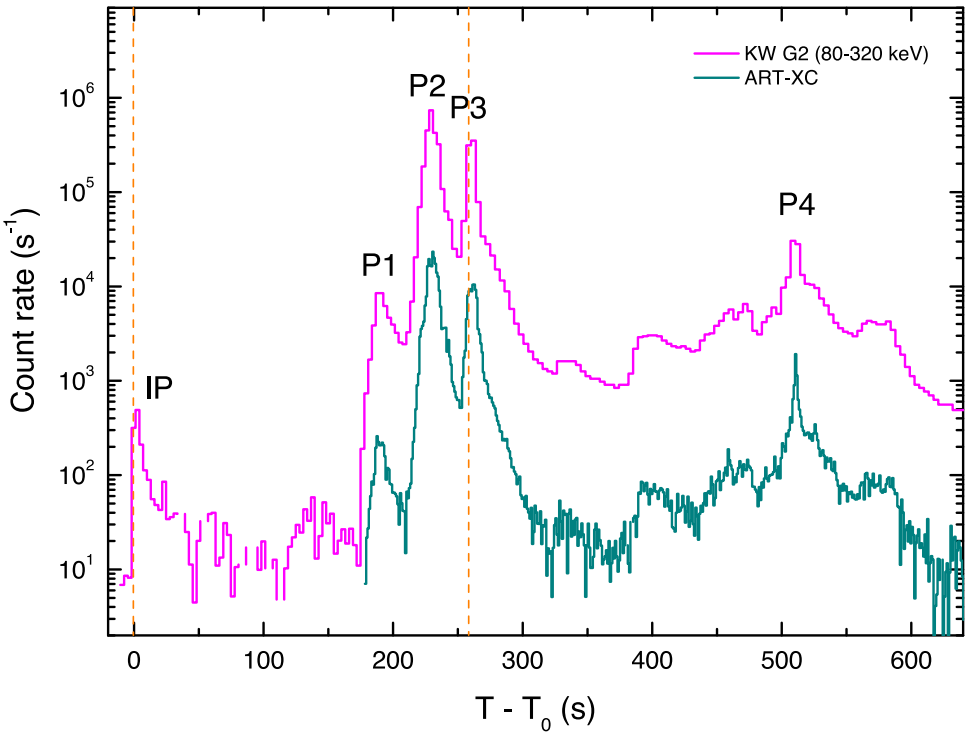


**Figure 1.** Overview of GRB 221009A prompt emission as observed by KW and ART-XC. The KW background-subtracted light curve, corrected for instrumental effects, is composed of THA, BGA, and HGA count rates in G2 (80–320 keV, the magenta line). The dark green line shows DT-corrected and background-subtracted ART-XC light curve in the full energy range 4–120 keV with the resolution of 1 s. Labels indicate the positions of the five peaks discussed in Section 3: the initial pulse (IP) and the four prominent peaks P1–P4 during the main phase. The KW triggered-mode data are available for the interval between two vertical dashed lines.

Spectral lags $\tau_{\rm lag}$ between the KW light curves are calculated with the method similar to that used in Frederiks et al. (2013).

### 2.2. ART-XC

ART-XC is a grazing-incidence-focusing X-ray telescope on board the Spectr-RG (SRG) observatory (Sunyaev et al. 2021). The telescope includes seven independent modules and has an FoV of 36′ in angular diameter. It provides imaging, timing, and spectroscopy in the 4–30 keV energy range with the total effective area of ∼450 cm$^2$ at 6 keV, angular resolution of 45″, energy resolution of 1.4 keV at 6 keV, and timing resolution of 23 $\mu$s (Pavlinsky et al. 2021). The primary purpose of ART-XC is to carry out the all-sky survey in hard X-rays with unprecedented sensitivity. At the same time, due to the high sensitivity and wide working energy range of the detectors (4–120 keV), ART-XC is able to detect high-energy events, such as solar flares or GRBs, from any direction in the sky (see, e.g., Levin et al. 2021).[5]

The instrument detected GRB 221009A at 13:19:55 UT on 2022 October 9. The burst happened outside its FoV, but its emission is well registered with all seven detectors. Due to the strong attenuation of the signal passed through the surrounding matter, ART-XC registers a light-curve shape that is practically not distorted by instrumental effects such as pulse pileup or flux saturation.

The telescope structure is designed in such a way that X-rays from celestial sources as well as cosmic background radiation are completely absorbed if coming not from the FoV. However, GRB 221009A came from about 30° off axis through the lateral surface of the structure of the instrument. This means that at least in the 4–60 keV energy range it did not detect the direct radiation from the burst but rather saw high-energy photons, whose energies were converted in the surrounding telescope structure by means of Compton scattering. Therefore, in the following analysis we use all photons registered by ART-XC in the energy range of 4–120 keV and correct count rates on DT and efficiency of CdTl detectors. The data from each module are analyzed separately, and then the results are combined.

## 3. Analysis and Results

Figure 1 shows the time history of GRB 221009A reconstructed from KW and ART-XC observations. The burst prompt emission has a complex time profile consisting of two distinct emission episodes. It starts with a single initial pulse (IP), which is followed, after a period of quiescence, by an extremely bright emission complex that lasts for ∼450 s and shows four prominent peaks: P1, at the onset; two huge pulses P2 and P3; and a much longer but less intense P4. After ∼600 s, the prompt, pulsed phase of the burst evolves to a steadily decaying, extended emission tail, which is visible in the KW data for more than 25 ks. Results of the KW spectral analysis are summarized in Table 1.

### 3.1. Initial Pulse

The light curve of the smooth, FRED-like IP, which triggered KW, resembles that of a typical long GRB. It starts at −1.8 s, peaks at ∼0.8 s, and decays to ∼30 s, with the G2 durations $T_{90}$ and $T_{50}$ of (29.9 ± 3.9) s and (10.4 ± 1.0) s, respectively.[6] The peak count rate is reached at $1.10 \times 10^3$ counts s$^{-1}$ in the 64 ms interval starting from 0.768 s.

[5] https://monitor.srg.cosmos.ru/

[6] $T_{90}$ and $T_{50}$ are the times to detect 90% and 50% of the observed count fluence, respectively.

**Table 1**
KW Spectral Fits to the Prompt Emission Spectra with the Band Function

| Spectrum | Time interval (s) | $\alpha$ | $\beta$ | $E_{\rm peak}$ (keV) | $\chi^2$/dof | Flux[a,b] (erg cm$^{-2}$ s$^{-1}$) |
|---|---|---|---|---|---|---|
| | | | Initial pulse | | | |
| 1–7 | 0.000–24.832 | $-1.62^{+0.05}_{-0.04}$ | <2.0 | $970^{+704}_{-330}$ | 80/98 | $1.03^{+0.21}_{-0.15} \times 10^{-6}$ |
| 1–5 | 0.000–8.448 | $-1.65^{+0.03}_{-0.03}$ | <2.0 | $1495^{+884}_{-448}$ | 89/94 | $2.58^{+0.40}_{-0.30} \times 10^{-6}$ |
| | | | P1 | | | |
| 27–58 | 180.480–208.640 | $-1.17^{+0.02}_{-0.02}$ | $-2.60^{+0.09}_{-0.12}$ | $1011^{+54}_{-54}$ | 181/97 | $3.64^{+0.04}_{-0.04} \times 10^{-5}$ |
| 35–41 | 186.624–188.416 | $-0.93^{+0.02}_{-0.02}$ | $-3.08^{+0.27}_{-0.48}$ | $1702^{+111}_{-110}$ | 58/79 | $1.11^{+0.05}_{-0.05} \times 10^{-4}$ |
| | | | P2 | | | |
| 59 | 208.640–216.832 | $-1.33^{+0.03}_{-0.03}$ | $-2.40^{+0.12}_{-0.18}$ | $981^{+112}_{-106}$ | 158/93 | $3.67^{+0.09}_{-0.09} \times 10^{-5}$ |
| 60 | 216.832–225.024 | $-1.18^{+0.08}_{-0.07}$ | $-2.49^{+0.05}_{-0.06}$ | $2733^{+141}_{-133}$ | 60/55 | $1.29^{+0.20}_{-0.18} \times 10^{-3}$ |
| 61[c] | 225.024–233.216 | $-0.76^{+0.05}_{-0.05}$ | $-2.13^{+0.02}_{-0.02}$ | $3038^{+120}_{-116}$ | 75/59 | $1.62^{+0.09}_{-0.09} \times 10^{-2}$ |
| 62 | 233.216–241.408 | $-0.86^{+0.06}_{-0.06}$ | $-2.78^{+0.04}_{-0.04}$ | $1617^{+32}_{-32}$ | 77/58 | $2.17^{+0.09}_{-0.09} \times 10^{-3}$ |
| 63 | 241.408–249.600 | $-1.25^{+0.04}_{-0.04}$ | $-2.75^{+0.05}_{-0.06}$ | $1072^{+32}_{-31}$ | 85/67 | $3.15^{+0.15}_{-0.15} \times 10^{-4}$ |
| | | | P3 | | | |
| 64 | 249.600–257.792 | $-0.97^{+0.07}_{-0.06}$ | $-2.51^{+0.04}_{-0.04}$ | $1886^{+73}_{-71}$ | 53/56 | $8.60^{+0.12}_{-0.12} \times 10^{-4}$ |
| | | | P1 + P2 + P3 | | | |
| 27–64[d] | 180.480–257.792 | $-0.89^{+0.06}_{-0.05}$ | $-2.21^{+0.02}_{-0.02}$ | $2660^{+109}_{-105}$ | 60/58 | $2.22^{+0.11}_{-0.10} \times 10^{-3}$ |

**Notes.**
[a] Averaged over the spectrum accumulation time interval.
[b] In the 20 keV–10 MeV band.
[c] "Peak" spectrum, used to calculate the peak energy flux.
[d] Time-averaged spectrum, used in calculation of the prompt emission fluence.

A time-averaged spectrum of the IP, measured from $T_0$ to 24.832 s, is best described by an exponentially cut off power law (CPL), parameterized as $E_p$: $f(E) \propto E^{\alpha} \exp(-E(2+\alpha)/E_p)$, with $\alpha \approx -1.62$ and $E_p \approx 970$ keV. A CPL fit to the spectrum near the peak count rate (from $T_0$ to 8.448 s) is characterized by a similar $\alpha \approx -1.65$ and the considerably higher $E_p \approx 1500$ keV. For both spectra, fits with the Band function are poorly constrained and set only an upper limit on the high-energy photon index ($\beta < -2.0$). The energy fluence of the IP is $(2.56 \pm 0.52) \times 10^{-5}$ erg cm$^{-2}$, and the 64 ms peak energy flux is $(6.20 \pm 1.52) \times 10^{-5}$ erg cm$^{-2}$ s$^{-1}$ (both in the 20 keV–10 MeV energy range).

For the IP, we derived statistically significant spectral lags ($\tau_{\rm lag}$) between the 64 ms light curves in G3 and G2 ($280 \pm 97$ ms) and between G3 and G1 light curves ($180 \pm 86$ ms). The positive spectral lags are indicative of hard-to-soft spectral evolution.

### 3.2. The Main Phase

During about 150 s after the end of the IP, the emission barely exceeds the background level, with only a hint of a wide bump around ∼150 s in the KW light curve. The main phase of the event begins at 175 s with a fast rise of the emission intensity to the peak P1 around 188 s (with the peak count rate of $\sim 1 \times 10^4$ counts s$^{-1}$, or 10x the IP), then temporary decays to $\sim 2 \times 10^3$ counts s$^{-1}$ around 208 s, the minimum between P1 and P2. A time-averaged spectrum of this pulse, measured from 180.48 s to 208.64 s, is best described by a Band function with $\alpha \approx -1.17$, $\beta \approx -2.60$, and $E_p \approx 1010$ keV.

The brightest phase of the burst (from ∼208 s to ∼280 s) is shown in Figure 2. Two huge pulses P2 and P3 contain about ∼90% (∼60% and ∼30%, respectively) of the total burst counts recorded in both the KW and ART-XC light curves. In the KW G2 band (and in the combined G1+G2+G3 band 20–1220 keV), the enormous peak count rate of $\sim 9.6 \times 10^5$ counts s$^{-1}$ ($\sim 2.2 \times 10^6$ counts s$^{-1}$) is reached in a 1 s interval around $T_{\rm peak} = 230$ s, at the second peak of the double-peaked P2. The ART-XC light curve shows a similar pattern, with the 1 s peak count rate of $\sim 2.7 \times 10^4$ counts s$^{-1}$. The emission at this phase is not only extremely intense but also spectrally hard: for the first time in KW GRB observations, a statistically significant (>60 $\sigma$) excess over the background is detected in the instrument's Z channel (∼16.5–22 MeV), which lasts for about 10 s and peaks, at ∼2400 counts/s, at the same time as the sub-MeV emission.

Spectral fits during the brightest phase are made using the pileup- and saturation-corrected THA (20–1220 keV) and PHA2 (0.4–16.5 MeV) data, and, at the highest peak, the DT-corrected Z-channel data (Figure 3). PHA1 data cannot be used due to the unrecoverable instrumental effects arising at such enormous fluxes (Appendix A.2). The two lower panels in Figure 2 show the spectral evolution of the emission: $E_p$ rises from ∼1 MeV between P1 and P2 to ∼3 MeV around the peak count rate, then drops back to ∼1 MeV between P2 and P3, and rises again to ∼2 MeV during the first ∼1/3 of the second huge pulse P3 (the last spectrum measured by KW). The temporal evolution of the low-energy photon index $\alpha$ shows a similar pattern, which is consistent with a positive correlation between the emission intensity and its spectral hardness.

After the peak of P3 around 260 s, the burst intensity starts to drop drastically (nearly to the pre-event level in ART-XC) but then increases again. The final, less bright phase of the prompt emission (P4) has a long (∼300 s), complicated structure, with the narrow count-rate maximum around 510 s. This part of the event was observed by KW in a single energy band (G2), making its spectral analysis impossible.

For the main phase, and given the relative weakness of IP, for the whole prompt emission, durations $T_{90}$ and $T_{50}$ in the KW 80–320 keV band are $284.0 \pm 3.7$ s and $31.1 \pm 3.7$ s, respectively. Estimated from the ART-XC ligt curve, the durations are very similar, $T_{90} = 276.0 \pm 5.4$ s and $T_{50} = 31.0 \pm 1.4$ s.

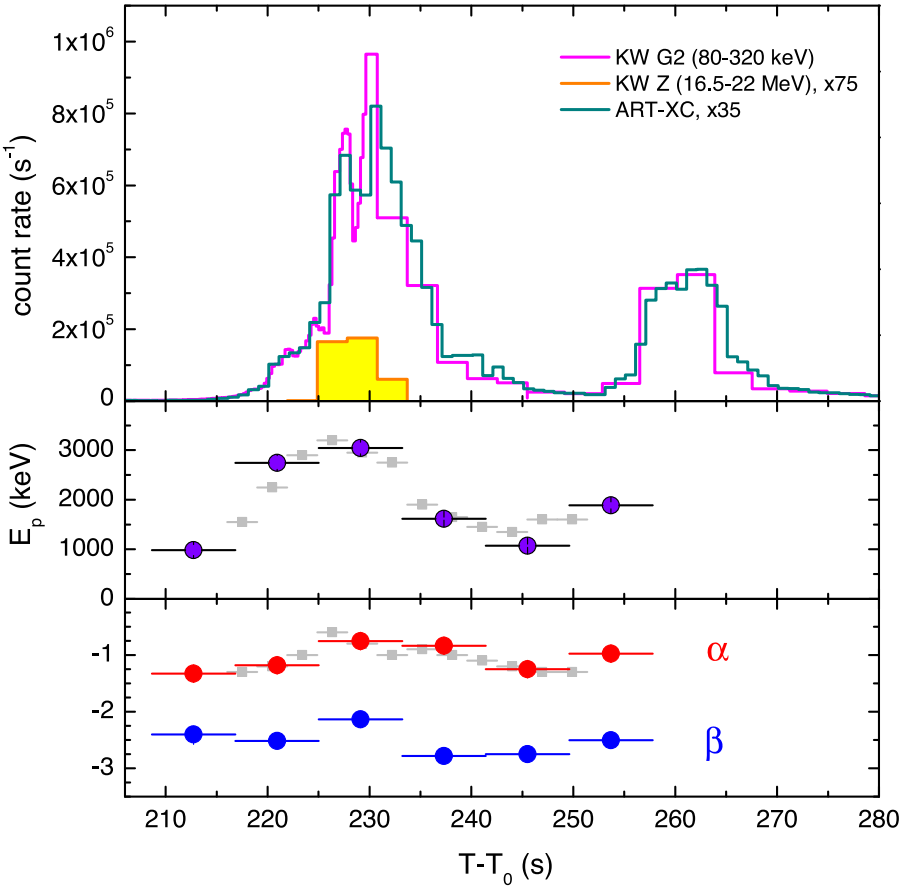


**Figure 2.** Brightest phase of GRB 221009A (pulses P2 and P3). The upper panel shows the light curve as seen by KW in G2 (80–320 keV, DT- and pileup-corrected count rate, magenta), ART-XC (DT-corrected count rate times 35, dark green), and by KW in the *Z* band (16.5–22 MeV, DT-corrected count rate times 75, orange/yellow). Middle panel: temporal evolution of the spectral peak energy $E_p$ as derived from the KW spectral fits with the Band function (Table 1). Lower panel: the evolution of the model photon indices: low-energy $\alpha$ (red) and high-energy $\beta$ (blue). For the spectral parameters, statistical errors are within the data points. Gray points illustrate $E_p$ and $\alpha$ estimates obtained from the KW light-curve data (Appendix A.1).

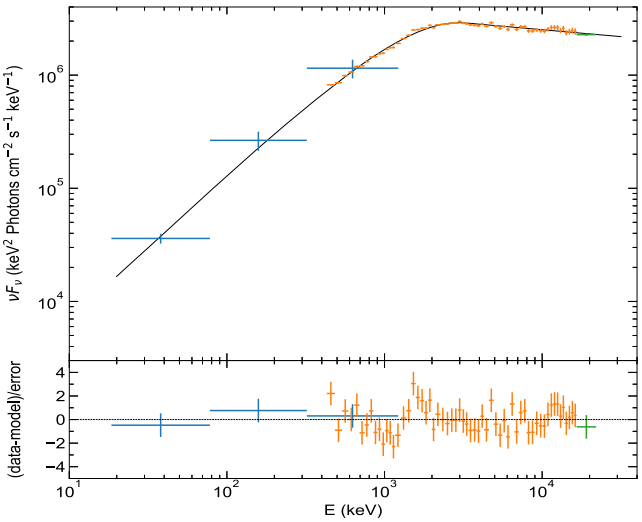


**Figure 3.** $\nu F_\nu$ spectrum at the peak of the prompt emission (225–233 s). Blue points represent pileup- and saturation-corrected THA data; orange points: pileup- and saturation-corrected PHA2 data; and the green point: DT-corrected Z-channel data (16.5–22 MeV). The best spectral fit with the Band function (Table 1) is shown with the solid line.

### 3.3. Observer-frame Energetics in the Prompt Emission

A time-averaged spectrum of the main phase of the prompt emission (180 to 258 s; Table 1) is best described by a Band function with $\alpha \approx -0.89$, $\beta \approx -2.21$, and $E_p \approx 2660$ keV. From this spectrum, the energy fluence measured up to the end of the KW triggered mode is $(0.172 \pm 0.015)$ erg cm$^{-2}$. Using the KW count-to-fluence ratio for the last recorded spectrum and assuming that the emission hardness during the remaining part of P3 is not much different, we calculate the overall fluence in P1+P2+P3 to be $(0.21 \pm 0.017)$ erg cm$^{-2}$.

The lack of KW spectral data for P4 does not allow us evaluate its fluence directly. Therefore, using the fraction of the total KW counts in this pulse (∼10%) and under the assumption that emission at this stage is likely softer than in the huge peaks (e.g., Kann & Agui Fernandez 2022), we account for the P4 contribution by adding 5% (≈0.01 erg cm$^{-2}$) to the P1+P2+P3 fluence and 2.5% systematic to the uncertainty. As a result, we obtain the total energy fluence of the prompt emission $S = (0.22 \pm 0.02)$ erg cm$^{-2}$ (0–600 s, 20 keV–10 MeV).

The spectrum at the brightest emission peak (225.024—233.216 s) is best fit with $\alpha \approx -0.76$, $\beta \approx -2.13$, and $E_p \approx 3040$ keV. From this spectrum and a peak-to-average count-rate ratio in the combined G1+G2+G3 light curve[7] we calculate the 20 keV–10 MeV peak energy flux of the burst $F_p = (3.14 \pm 0.47) \times 10^{-2}$ erg cm$^{-2}$ s$^{-1}$ (or $\sim 1.4 \times 10^4$

[7] Calculations using the KW spectrum and the ART-XC light curve yield a very similar $F_p$ value.

photons $\mathrm{cm}^{-2}\,\mathrm{s}^{-1}$) in a 1 s interval starting from 229.632 s. As for the exceptionally high count rate, the derived $F_{\rm p}$ is the highest among >3500 GRBs detected by the KW so far.

### 3.4. Early Afterglow

The prompt, pulsed phase of the burst ends at ∼600 s, when the light curve evolves to a steadily decaying emission tail, which is below the sensitivity of ART-XC but is visible in the KW data for more than 25 ks (Figure 4(a)). In the KW G2 band, the decay in the interval from 650 s to 25.7 ks is well described by a simple power law (PL) $N(t) \propto (t - T_0)^{-\alpha_t}$ with the PL index $\alpha_{\rm t} = 1.69 \pm 0.03$ ($\chi^2$=16/14 degrees of freedom, hereafter dof), while a broken PL (BPL) fit to the data is not constrained.

Starting from 5.1 ks, count rates in all three bands (G1, G2, and G3) are available that allows estimating emission spectrum. From a PL fit to a three-channel spectrum constructed for the time interval from 5.1 ks to 25.7 ks, we obtain the photon index $\Gamma = 1.99 \pm 0.05$ and time-averaged flux $1.10^{-0.06}_{-0.08} \times 10^{-8}$ erg $\mathrm{cm}^{-2}\,\mathrm{s}^{-1}$ (20–1500 keV). Assuming a PL spectrum with $\Gamma = 2$, we estimate the 20 keV–10 MeV energy fluence of the GRB 221009A extended emission from 650 s to 25.7 ks to be $(2.15 \pm 0.14) \times 10^{-3}$ erg $\mathrm{cm}^{-2}$, or ≈1% of the energy in the prompt phase of the burst. Using the late-time spectrum, we extrapolate KW flux points after ∼5 ks to the 0.3–10 keV band and find them consistent, within a factor of ∼1.3, with unabsorbed fluxes derived from simultaneous XRT observations.[8]

The combination of the spectral and temporal behaviors of the steadily decaying emission is in reasonable agreement with that expected at the "normal" (III) phase of the canonical X-ray afterglow (Nousek et al. 2006; Zhang et al. 2006; Racusin et al. 2009) and supports a scenario in which the bright, extended γ-ray emission observed by KW is generated by the synchrotron forward-shock mechanism during the normal spherical decay of the afterglow (Mészáros & Rees 1997). It should be noted, however, that the use of $T_0$, corresponding to the early and relatively weak precursor, as a zero time point ($t_0$) of the bright afterglow can barely be justified, and the decay slope measured at times not much larger than $T_{90}$ could be very sensitive to the assumed $t_0$ (the "$t_0$ effect"; Zhang et al. 2006).

Therefore, in order to characterize the afterglow temporal behavior more precisely and to identify a possible break, we performed temporal PL and BPL fits with $t_0$ set to several characteristic times in the GRB 221009A light curve: $T_{\rm peak} = 230$ s, the peak time of the prompt emission; 370 s, the light-curve minimum between the brightest phase (P2+P3) and the last episode of the prompt emission (P4); 510 s, the peak time of P4; and, finally, 650 s, the time when the steadily decaying afterglow starts to dominate the observed flux.

The results of our fits with different zero time points are presented in Table 2 and Figure 4. The choice of $T_{\rm peak}$ as $t_0$ does not constrain a break and results in a more gentle, as compared to $t_0 = 0$, PL slope $\alpha_{\rm t} = -1.50 \pm 0.04$. This index is in perfect agreement with the soft X-ray slope of ≈1.5 between ∼3 ks and ∼80 ks (O'Connor et al. 2023; Williams et al. 2023), and it also fits better in the slope range of the "normal" afterglow segment ($1 < \alpha_t < 1.5$).

[8] Unabsorbed Swift-XRT fluxes were extracted from the XRT repository (Evans et al. 2007, 2009).

With the shift of $t_0$ toward the end of the prompt emission, a broken PL shape becomes preferred by the data: the break significance increases from ∼2.5σ ($t_0 = 370$ s) to ∼4σ ($t_0 = 510$ s) and ∼10.5σ ($t_0 = 650$ s). In the two latter cases, the combination of a shallow pre-break slope $\alpha_{1,\rm t} \sim 0.51 - 0.86$ and the steeper post-break slope $\alpha_{2,\rm t} \sim 1.6$ closely resembles that of the transition from the "plateau" (Segment II) to the "normal" phase of the canonical X-ray afterglow. The break positions, located in a narrow time interval of the light curve (2100–2600 s relative to $T_0$), are also in the range expected for a break from Segment II to Segment III ($10^3$–$10^4$ s). We note that using $\sim T_0 + 510$ s as a reference time point when fitting the late-time GBM light curve, Lesage et al. (2023) obtained a similar index to the KW PL index (∼0.82) for the decay from 650 s to 1460 s after the trigger (after that time GRB 221009A is occulted by Earth for Fermi); and also the post-break KW index is consistent with the early soft X-ray slope of ≈1.5 noticed above in this Section.

## 4. Discussion

### 4.1. Prompt Emission in Context

GRB 221009A is the brightest GRB observed by KW in almost 30 yr of observations. The incident photon flux, peaking at $\gtrsim 2 \times 10^6$ $\mathrm{s}^{-1}$, was previously exceeded only in KW detections of giant flares from Galactic magnetars SGR 1900 + 14 (on 1998 August 27; Mazets et al. 1999b) and SGR 1806-20 (2004 December 27; Frederiks et al. 2007) and is comparable to that in the extremely bright flare from SGR 1627-41 (1998 June 18; Mazets et al. 1999a).

Since the launch in 1994 November and up to 2023 February, KW has detected ∼3570 GRBs with virtually no bright GRBs having been missed. About ∼85% of them are long-duration bursts. To compare GRB 221009A with the bright KW GRB population, we have selected ∼150 long bursts with $S \gtrsim 10^{-4}$ erg $\mathrm{cm}^{-2}$. In this sample, GRB 130427A has the largest fluence $3 \times 10^{-3}$ erg $\mathrm{cm}^{-2}$, and GRB 140219A is the brightest in terms of the peak energy flux ($1.2 \times 10^{-3}$ erg $\mathrm{cm}^{-2}\,\mathrm{s}^{-1}$). Ten percent of the most fluent bursts have durations ranging from 10 s (GRB 021206) to 680 s (GRB 160625B) and $E_p$ of time-integrated spectra between ∼550 keV (GRB 160625B) and ∼2500 keV (GRB 140219A). The KW ultra-long GRBs (22 bursts with a duration ≳1000 s) have moderate spectral hardness, with typical $E_p$ of a few hundred keV, which yield moderate fluences below $6 \times 10^{-4}$ erg $\mathrm{cm}^{-2}$. Thus, GRB 221009A is at the extreme end of the bright GRB population being simultaneously very long-duration and hard-spectrum. A more detailed analysis of GRB 221009A in the context of the bright GRB population is presented in a separate paper (Burns et al. 2023).

### 4.2. Rest-frame Energetics and Prompt Hardness–Intensity Correlations

Using $z = 0.151$ and the values of the total energy fluence $S$ and the peak energy flux $F_p$ in the observer frame (Section 3.3), we estimate the rest-frame energetics of the burst prompt emission. Assuming a ΛCDM cosmological model with $\Omega_M = 0.308$, $\Omega_\Lambda = 0.692$, and $H_0 = 67.8$ km $\mathrm{s}^{-1}$ $\mathrm{Mpc}^{-1}$ (Planck Collaboration et al. 2016), $E_{\rm iso}$ is $(1.2 \pm 0.1) \times 10^{55}$ erg, and the peak isotropic luminosity $L_{\rm iso}$ is $(2.1 \pm 0.4) \times 10^{54}$ erg $\mathrm{s}^{-1}$ (on the 1 s scale). By applying a typical, for KW long GRBs, 1024 ms $F_p$ to 64 ms $F_p$ conversion factor of 1.71, the 64 ms $L_{\rm iso}$

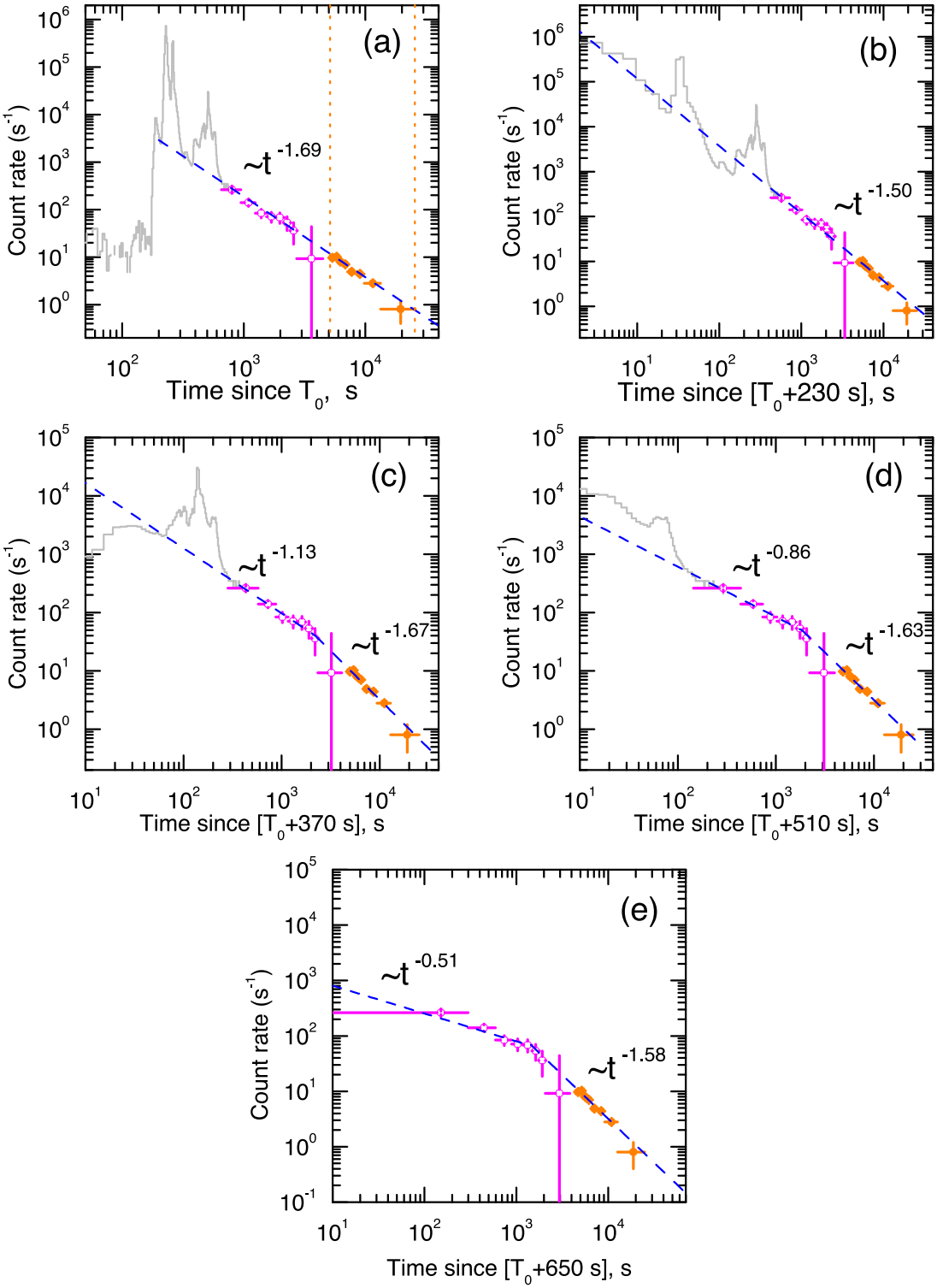


**Figure 4.** Early afterglow of GRB 221009A observed by KW in the 80–320 keV band. Magenta points: time-averaged HGA data. Orange points: time-averaged BGA data. The interval from 5.1 to 25.7 ks (the vertical dotted lines in panel (a)) is used for the late-time spectral fit. Dashed lines in each panel show the best PL (or the best BPL) temporal fit to the data in the interval from 650 s to 25.7 ks after the trigger. Zero time points of the fits are specified in the *x*-axis labels. The prompt emission light curve (gray solid lines) is shown for the reference.

is estimated to be $(3.4 \pm 0.5) \times 10^{54}$ erg s$^{-1}$. The reported energetics are calculated in the bolometric rest-frame range 1 keV–10 MeV. Derived from the observer-frame $E_p$ values (Section 3.3), the rest-frame spectral peak energies $(1+z)\,E_p$ are $E_{\rm p,i,z} \approx 2900$ keV (time-averaged) and $E_{\rm p,p,z} \approx 3500$ keV (at the peak luminosity).

These estimates make GRB 221009A the most energetic and the third-most luminous $\gamma$-ray burst observed since the beginning of the cosmological era in 1997.[9] Figure 5 shows

[9] After GRB 110918A (Frederiks et al. 2013) and GRB 210619B (Svinkin et al. 2021).

**Table 2**
KW Temporal Power-law Fits to the Early Afterglow

| $t_0$ | Model | $\alpha_t$ | $\alpha_{1,t}$ | $\alpha_{2,t}$ | $t_b$ (s) | $\chi^2$/dof |
|---|---|---|---|---|---|---|
| 0 | PL | $1.69^{+0.03}_{-0.03}$ | ... | ... | ... | 16/14 |
| 230 s | PL | $1.50^{+0.04}_{-0.04}$ | ... | ... | ... | 14/14 |
| 370 s | PL | $1.36^{+0.02}_{-0.02}$ | ... | ... | ... | 23/14 |
| 370 s | BPL | ... | $1.12^{+0.10}_{-0.10}$ | $1.67^{+0.12}_{-0.09}$ | $2200^{+870}_{-540}$ | 9/12 |
| 510 s | PL | $1.20^{+0.02}_{-0.02}$ | ... | ... | ... | 31/14 |
| 510 s | BPL | ... | $0.86^{+0.08}_{-0.08}$ | $1.63^{+0.11}_{-0.09}$ | $1840^{+550}_{-370}$ | 8/12 |
| 650 s | PL | $0.88^{+0.01}_{-0.01}$ | ... | ... | ... | 141/14 |
| 650 s | BPL | ... | $0.51^{+0.04}_{-0.04}$ | $1.58^{+0.10}_{-0.09}$ | $1440^{+300}_{-250}$ | 9/12 |

**Note.** The fits are made in the time interval from 650 s to 25.7 ks and use $t_0$ as a zero time point. The model parameters are as follows: $\alpha_t$ is the simple PL index; $\alpha_{1,t}$ and $\alpha_{2,t}$ are BPL pre-break and post-break indices, respectively; and $t_b$ is the break time (with respect to $t_0$).

$E_{\rm iso}$ and $L_{\rm iso}$ for GRB 221009A along with the KW sample of more than 300 long GRBs with known redshifts (Tsvetkova et al. 2017, 2021). In the rest-frame hardness–intensity plane $E_{\rm p,i,z} - E_{\rm iso}$ GRB 221009A lies inside the 68% prediction interval of the "Amati" relation for the KW sample. Likewise, in the $E_{\rm p,p,z} - L_{\rm iso}$ plane, the burst perfectly fits the "Yonetoku" relation. From this, we conclude that GRB 221009A is most likely a very rare, very hard, super-energetic version of a "normal" long GRB.

### 4.3. Fundamental Plane Correlation between Prompt and Afterglow Emissions

In Section 3.4 we show that, with the zero time point shifted close to the end of the prompt emission, the broken PL behavior of the bright, early $\gamma$-ray afterglow observed by KW can be interpreted as the transition from Segment II (plateau phase) to Segment III (normal spherical decay phase) of the canonical X-ray afterglow. Based on this assumption, we test the rest-frame parameters of the prompt emission and the early afterglow against a three-dimensional relation between the peak prompt luminosity $L_{\rm peak}$, the rest-frame time at the end of the X-ray plateau, and its corresponding luminosity in X-rays $L_X$: the so-called 3D Dainotti fundamental plane relation (Dainotti et al. 2017; Dainotti et al. 2020). Given the most significant break position ($t_b = 1440$ s; $t_0 = 650$ s), $T_X^* = t_b/(1+z)$ is $\sim$1250 s and $L_X = 4\pi d_L^2 F_X = 4.0 \times 10^{49}$ erg s$^{-1}$, where $F_X = 6.0 \times 10^{-7}$ erg cm$^{-2}$ s$^{-1}$ is the X-ray flux at $t_b$, extrapolated from the KW band to the 0.3–10 keV band using the late-time KW spectrum.[10]

Using $T_X$*, $L_X$, and $L_{\rm peak} = L_{\rm iso}$ (1 s scale), we calculate a distance from GRB 221009A to the fundamental plane for the full sample of 222 GRBs studied in Dainotti et al. (2020) and to the planes for its "gold" (65 GRBs) and "long GRB" (129 events) subsamples. In each case, we find the distance within $1\sigma$ scatter of the tested relation, with the best agreement achieved for the "gold" and long GRB fundamental planes. This further supports the consistency of GRB 221009A properties with the less-energetic long GRB population.

[10] With the photon spectral index $\Gamma = 2$; for this spectrum cosmological $K$-correction is unity.

### 4.4. Collimation-corrected Energy and Central Engine

Long GRBs are thought to originate in the collapse of massive stars (Paczyński 1998; MacFadyen & Woosley 1999). The most widely discussed models of central engines are newborn, rapidly rotating compact objects, such as magnetars and black holes emitting highly collimated, ultra-relativistic jets (fireballs). When the tightly collimated relativistic fireball is decelerated by the circumburst medium down to the Lorentz factor $\approx 1/\theta_{\rm jet}$ ($\theta_{\rm jet}$ is the jet opening angle), an achromatic break (jet break) should appear, in the form of a sudden steepening in the GRB afterglow light curve, at a characteristic time $t_{\rm jet}$. When the opening angle of the jetted outflow is known, the isotropic-equivalent energetics can be converted to the more accurate collimation-corrected energetics (Sari et al. 1999).

Given $E_{\rm iso} = 1.2 \times 10^{55}$ erg and assuming a top-hat jet, the total collimation-corrected energy of GRB 221009A is $E_{\rm K} \approx 10^{53}$ erg $t_{\rm jet}^{3/4}$ $(\eta_\gamma/0.2)^{-3/4}$ $n_0^{1/4}$, where $n_0$ is the medium number density, $\eta_\gamma$ is the radiative efficiency of the prompt phase, and $t_{\rm jet}$ is measured in days. Although extensive multiwavelength follow-up of GRB 221009A did not reveal an apparent achromatic break in the afterglow light curve, a number of $\theta_{\rm jet}$ estimates are reported, ranging from $0\overset{\circ}{.}7$ to $>10\overset{\circ}{.}7$ (An et al. 2023; Kann et al. 2023; Negro et al. 2023; O'Connor et al. 2023; Williams et al. 2023), which, assuming typical $\eta_\gamma = 0.2$ and $n_0 = 1$ cm$^{-3}$, imply $E_{\rm K}$ from $\sim 5 \times 10^{51}$ to $\sim 5 \times 10^{53}$ and even higher.

The magnetar central-engine model, where the GRB is powered by a newborn, fast-rotating magnetar, predicts $E_{\rm K}$ below few $\times 10^{52}$ erg (see, e.g., Metzger et al. 2011), while the accreting black hole models extend the limit on the GRB total energetics up to $\sim 10^{54}$ erg (see, e.g., van Putten & Della Valle 2017). For GRB 221009A to match the total released energy consistent with the predictions of the black hole central-engine model, a collimation-correction factor of $\gtrsim 10$ is required, corresponding to a top-hat jet half-opening angle constraint of $\theta_{\rm jet} < 25^\circ$ or $t_{\rm jet} \lesssim 30$ days. The structured jet model suggested by O'Connor et al. (2023) allows even lower total energy of the explosion, below $\sim 10^{53}$ erg, which may fit magnetar central-engine models. Thus, despite the enormous isotropic energy implied, an energy budget of GRB 221009A can still be explained within a standard scenario for the central engine/progenitor of long GRBs.

A more detailed discussion of GRB 221009A collimated energetics is presented in Burns et al. (2023), including in the context of the KW sample.

### 4.5. Emission Feature around 10 MeV

Ravasio et al. (2023), hereafter R23, analyzed GBM spectral data outside the time interval affected by saturation (called Bad Time Interval, BTI; 219–277 s after the GBM trigger) and discovered a highly significant narrow emission feature on top of the prompt emission continuum. The spectral line, modeled by a Gaussian with a roughly constant width $\sim$1 MeV and a central energy $E_{\rm line}$ decreasing in time from $\sim$12.5 to $\sim$6 MeV, is detected at $>6\sigma$ in the interval from 280 to 320 s (the decay phase of the second huge pulse P3) and nondetected before BTI (including the interval 184–216 s at the rising front of the

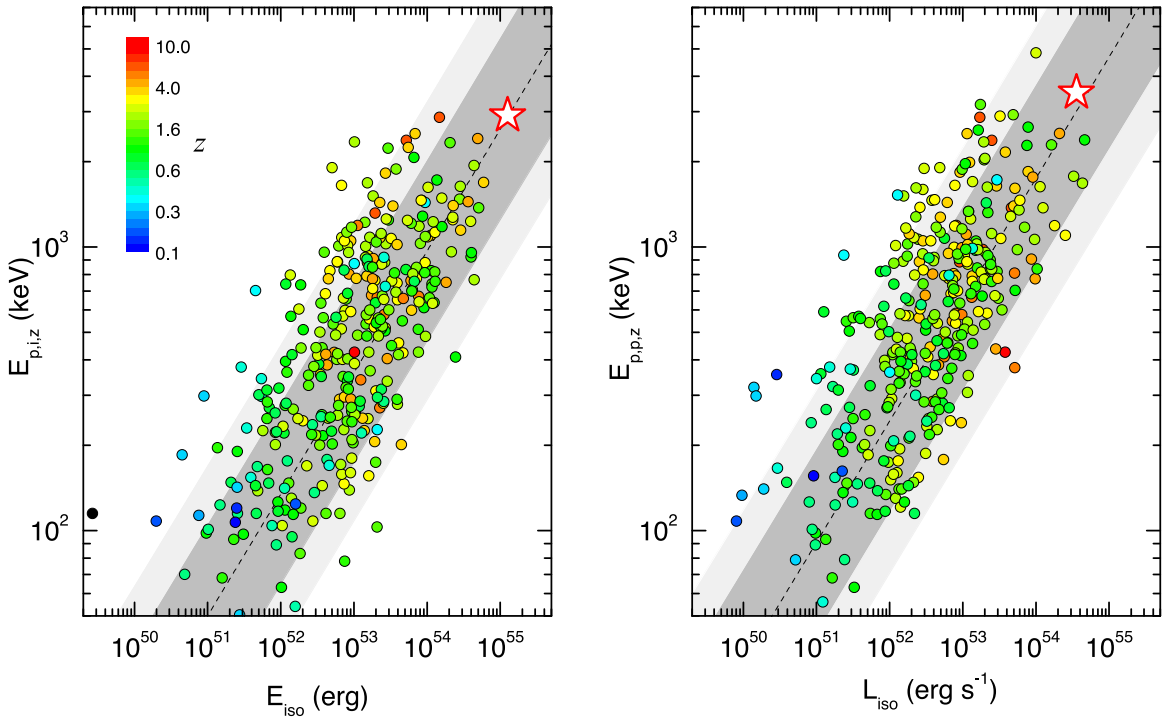


**Figure 5.** Rest-frame energetics of GRB 221009A in the $E_{p,i,z}$–$E_{iso}$ and $E_{p,p,z}$–$L_{iso}$ planes (stars). The rest-frame parameters of 315 long KW GRBs with known redshifts (Tsvetkova et al. 2021) are shown with circles; the color of each data point represents the burst's redshift. The "Amati" and "Yonetoku" relations for this sample are plotted with dashed lines, and the dark- and light-gray shaded areas show their 68% and 90% prediction intervals, respectively. The error bars are not shown here for reasons of clarity.

brightest phase of the burst). R23 interpret this feature as a blueshifted electron–positron annihilation line of relatively cold electron–positron pairs, which could have formed within the jet region where the brightest pulses of the GRB were produced.

Among the many $\gamma$-ray detectors that observed GRB 221009A, KW is one of the few instruments capable of making detailed spectral measurements at energies around 10 MeV, and its independent identification of the spectral line reported from GBM data would be of obvious importance. Unfortunately, the time span of KW spectral measurements ends $\sim$20 s before the time range of the spectral line detection reported in R23. However, KW spectral data on the brightest part of the burst, corrected for pileups and saturations, can be tested for the presence of a similar spectral feature.

We visually inspect best-fit residuals for five KW spectra covering the interval from 217 to 257 s, and only in one, measured at the very peak of the emission (225 to 233 s), we find a marginal ($\lesssim 2\sigma$) excess in the count rate over the fitted continuum in the region around 10 MeV. Although this excess is not alone in this spectrum (there is another one around 1.8 MeV), and the systematic variations in the fit residuals may be, among other reasons, due to a spectral evolution of the emission during the 8 s accumulation interval, we analyze the spectrum for the presence of a statistically significant feature similar to that of R23.

For this purpose, we model the excess by adding a Gaussian line (XSPEC model `gauss`), with initial $E_{line}$=10 MeV and width fixed to 1 MeV,[11] to the best-fit continuum for this spectrum. Our fit with the combined model results at only a marginal improvement in the statistic ($\Delta\chi^2 = 6.7$ for two additional dof) in $E_{line} = 14.65^{+0.86}_{-0.69}$ MeV and the total photon flux in the line of $5.9^{+2.4}_{-2.3}$ ph cm$^{-2}$ s$^{-1}$, which implies the line isotropic luminosity $L_{line} \sim 9.2 \pm 3.8 \times 10^{51}$ erg s$^{-1}$. We estimate the improvement significance by applying the Akaike Information Criterion (see, e.g., Burnham & Anderson 2004), the method employed by R23, and find that the addition of the Gaussian line to the model results in only a small decrease in the value of the criterion $\Delta$AIC $\approx 2.7$ that corresponds to $<1\sigma$ significance of the improvement.

Nevertheless, we note that the estimated line central energy fits well the decaying trend of $E_{line}$ reported in R23, and the implied ratio $L_{line,51}/(E_{line}/1\,\mathrm{MeV}) \sim 0.63$ is in the range, predicted at times close to the emission peak by one of the emission scenarios explored by the authors, which involves high-latitude emission from the shell that produced the most luminous pulse in the GRB light curve.

This work is supported by RSF grant 21-12-00250. S.M. and A.A.L. acknowledge the support by the RFBR grant 19-29-11029 in the part of the ART-XC data analysis. This work made use of data supplied by the UK Swift Science Data Centre at the University of Leicester.

*Facilities:* Wind (Konus), SRG (ART-XC).

## Appendix A
## Konus-WIND Data Corrections

### *A.1. Light Curves*

A standard KW DT-correction procedure for light curves is a simple non-paralyzable DT correction in each of the measurement bands, with a DT $\tau$ of $\sim 4\mu$s, taking into account a softer gate blocking by harder ones. This method, based on a relation $1/n + 1/N = \tau$ between the total photon flux $N$ incident on the detector (assuming 100% detection efficiency) and the recorded

[11] Fits with line width left free are not constrained.

count rate $n$, provides a robust flux estimate for $N \lesssim 1/\tau$ ($\sim 2.5 \times 10^5$ cts s$^{-1}$). At $N \gg 1/\tau$, $n$ ceases to depend on $N$ (saturates), and the standard DT correction becomes ineffective.

At very high incident fluxes, pulse pileups in detector electronics lead to multiple analog and digital distortion effects that require special efforts to correctly reconstruct the time history of the event and the energy spectra. The instrument response to fluxes up to $10^6$–$10^7$ cts s$^{-1}$ of various incident photon spectra was studied in laboratory experiments with strong radioactive and X-ray sources, as well as in Monte Carlo simulations of KW analog and digital electronics behavior (Mazets et al. 1999b). It was found that the pattern of the pileup-distorted $n(N)$ relations for each of the three energy bands G1, G2, and G3 is strongly sensitive to the shape of the incident photon spectrum. Hence, by comparing the behavior of observed rates $g_{1,2,3}$ (in G1, G2, and G3, respectively) with the $n_{1,2,3}(N)$ dependencies obtained from simulations for different energy spectra, one can reliably reconstruct not only the incident emission intensity but also its spectral shape. Based on this approach, deconvolution procedures were developed that allowed, e.g., to successfully recover time histories and energy spectra of extremely bright magnetar flares (Mazets et al. 1999a; Mazets et al. 1999b).

To reconstruct GRB 221009A light curves in the triggered detector S2 at the peak of the emission, we, following the approach of Mazets et al. (1999b), performed Monte Carlo simulations for various incident count fluxes $N$ and Band-shaped photon spectra, forward-folded with the detector response matrix. From the simulations, we obtained a database of $\sim$10,000 $n_i(N, \alpha, \beta, E_p)$ dependencies for $N$ up to $\sim 4 \times 10^7$ s$^{-1}$, $\alpha$ in range $(-1.8, +1.0)$, $\beta$ in range $(-3.0, -2.0)$, and $E_p$ in the range from 500 keV to 4.5 MeV.

Then, for each time bin in the interval from 216 s to 250 s, we searched the database for the best match of a simulated triplet $n_{1,2,3}(N, \alpha, \beta, E_p)$ and the measured rates $g_{1,2,3}(t)$ by minimizing the sum in quadrature of normalized differences $(n_i(N, \alpha, \beta, E_p) - g_i(t))/g_i(t)$. In order to reduce the number of free spectral parameters in the search, $\beta(t)$ was fixed to that obtained from a preliminary fit to the corresponding multichannel spectrum in the PHA2 band (0.4–16.5 MeV); this approach is justified by the fact that the hard end of the KW instrumental spectrum (at energies above $\sim$2–4 MeV) remains nearly undistorted by pileups, and hence, the high-energy spectral index can be estimated independently. In a case of ambiguous identification, we manually selected the best-solution parameters ($N$, $\alpha$, $E_p$) using the following criteria. First, the variation of the emission intensity ($N$) over time had to follow its general course in the second KW detector S1, for which, for this GRB, saturation and pileup effects are negligible due to the emission absorption in the Wind body and the rear structure of the detector. Second, we aimed to achieve smooth variations in the spectral parameters $\alpha$ and $E_p$ over time. Finally, using the best-solution parameters ($\alpha(t)$, $\beta(t)$, $E_p(t)$), we calculated a Band-shaped spectrum, normalized on the incident count flux $N(t)$ in the whole instrument energy range, and reconstructed count rates Gi ($t$) were calculated, from this spectrum, as count fluxes in the corresponding energy band Gi.

As a result, we obtained the reconstructed incident count rates as well as time-resolved estimates of the spectral parameters (illustrated in Figure 2). To estimate uncertainties in these values, we performed simulations by varying (assuming Poisson-distributed counts) the measured rates for several time bins. The resulting variations in the best-solution parameters do not exceed $\sim$0.15 for $\alpha$, $\sim$10% for $E_p$, and about 18% for the flux $N$.

### A.2. Multichannel Spectra

A standard KW DT-correction procedure for multichannel spectra is similar to that for the light curves but with about 10 times longer $\tau \approx 42\mu$s. Accordingly, count rate saturations in PHA1 and PHA2 are not negligible at $N \gtrsim 2.4 \times 10^4$ s$^{-1}$, and pileup corrections become necessary at $N \gtrsim 5 \times 10^4$ s$^{-1}$ (in the corresponding spectral band). The influence of the pileup effect on KW spectra was examined in studies of powerful solar flares (Lysenko et al. 2019, 2022). An iterative correction method for pileup-distorted spectra was developed that allowed, e.g., to recover, at incident count rates up to $\sim 2 \times 10^5$ cts s$^{-1}$, steep, broken PL spectral shapes to the accuracy of $\sim$0.1 in the spectral indices and $\sim$10 keV in the break energy. In these studies, spectral shape corrections were applied to PHA1 (20–1200 keV), whereas the flux was corrected using joint spectral fits with nearly undistorted and unsaturated spectra in the PHA2 range (0.4–16.5 MeV).

For GRB 221009A, both saturation and pileup corrections are necessary to three 8.192 s long spectra measured from 216.832 to 241.408 s after the trigger. In this time interval, a huge incident flux in the PHA1 band (up to millions counts/s) makes corrections with a method similar to that of Lysenko et al. (2019) very difficult, if not impossible. However, such a procedure is still applicable to spectra in the PHA2 band, where incident rates do not exceed $\sim 3 \times 10^5$ cts s$^{-1}$, but an "external" normalization is still required to correct the deeply saturated measured flux. The flux corrections were performed by simultaneous fits of the shape-corrected PHA2 spectra with three spectral points in the 20–1200 keV band, constructed from the light-curve data, which were corrected independently (see Appendix A.1).

For the spectrum at the peak of the emission (225.024–233.216 s after the trigger), an additional spectral point is available from the unsaturated Z-channel data (16.5–22 MeV), thus providing an independent reference at higher energies. For this spectrum, joint fits were made to three data sets: THA+PHA2; PHA2 + Z; and THA+PHA2 + Z. The fits result in very similar spectral parameters and fluxes, which confirms the correctness of our approach to recover both the pileup-distorted shape of the spectrum and the saturated incident flux.

## ORCID iDs

D. Frederiks https://orcid.org/0000-0002-1153-6340
D. Svinkin https://orcid.org/0000-0002-2208-2196
A. L. Lysenko https://orcid.org/0000-0002-3942-8341
S. Molkov https://orcid.org/0000-0002-5983-5788
A. Tsvetkova https://orcid.org/0000-0003-0292-6221
M. Ulanov https://orcid.org/0000-0002-0076-5228
A. Ridnaia https://orcid.org/0000-0001-9477-5437
A. A. Lutovinov https://orcid.org/0000-0002-6255-9972

## References

Abdo, A. A., Ackermann, M., Arimoto, M., et al. 2009, Sci, 323, 1688
Amati, L., Frontera, F., Tavani, M., et al. 2002, A&A, 390, 81

Amati, L., Guidorzi, C., Frontera, F., et al. 2008, MNRAS, 391, 577
An, Z.-H., Antier, S., Bi, X.-Z., et al. 2023, arXiv:2303.01203
Aptekar, R. L., Frederiks, D. D., Golenetskii, S. V., et al. 1995, SSRv, 71, 265
Arnaud, K. A. 1996, in ASP Conf. Ser. 101, Astronomical Data Analysis Software and Systems V, ed. G. H. Jacoby & J. Barnes (San Francisco, CA: ASP), 17
Atteia, J. L., Boër, M., & Hurley, K. 1999, A&AS, 138, 421
Atteia, J. L., Heussaff, V., Dezalay, J. P., et al. 2017, ApJ, 837, 119
Band, D., Matteson, J., Ford, L., et al. 1993, ApJ, 413, 281
Belkin, S., Kim, V., Pozanenko, A., et al. 2022a, GCN, 32769, 1
Belkin, S., Moskvitin, A., Kim, V., et al. 2022b, GCN, 32818, 1
Bissaldi, E., Omodei, N., Kerr, M. & Fermi-LAT Team 2022, GCN, 32637, 1
Briggs, M. S., Paciesas, W. S., Pendleton, G. N., et al. 1996, ApJ, 459, 40
Burnham, K. P., & Anderson, D. R. 2004, Sociol Methods Res, 33, 261
Burns, E., Svinkin, D., Fenimore, E., et al. 2023, ApJL, 946, L31
Castro-Tirado, A. J., Sanchez-Ramirez, R., Hu, Y. D., et al. 2022, GCN, 32686, 1
Dado, S., & Dar, A. 2022, ApJL, 940, L4
Dainotti, M. G., Hernandez, X., Postnikov, S., et al. 2017, ApJ, 848, 88
Dainotti, M. G., Lenart, A. Ł., Sarracino, G., et al. 2020, ApJ, 904, 97
de Ugarte Postigo, A., Izzo, L., Pugliese, G., et al. 2022a, GCN, 32648, 1
de Ugarte Postigo, A., Izzo, L., Thoene, C. C., et al. 2022b, GCN, 32800, 1
Dichiara, S., Gropp, J. D., Kennea, J. A., et al. 2022, GCN, 32632, 1
Evans, P. A., Beardmore, A. P., Page, K. L., et al. 2007, A&A, 469, 379
Evans, P. A., Beardmore, A. P., Page, K. L., et al. 2009, MNRAS, 397, 1177
Frederiks, D., Lysenko, A., Ridnaia, A., et al. 2022, GCN, 32668, 1
Frederiks, D. D., Golenetskii, S. V., Palshin, V. D., et al. 2007, AstL, 33, 1
Frederiks, D. D., Hurley, K., Svinkin, D. S., et al. 2013, ApJ, 779, 151
Frontera, F., Guidorzi, C., Montanari, E., et al. 2009, ApJS, 180, 192
Ghirlanda, G., Nava, L., Ghisellini, G., & Firmani, C. 2007, A&A, 466, 127
Goldstein, A., Preece, R. D., Mallozzi, R. S., et al. 2013, ApJS, 208, 21
Gotz, D., Mereghetti, S., Savchenko, V., et al. 2022, GCN, 32660, 1
Greiner, J., Clemens, C., Krühler, T., et al. 2009, A&A, 498, 89
Gruber, D., Greiner, J., von Kienlin, A., et al. 2011, A&A, 531, A20
Guidorzi, C., Lacapra, M., Frontera, F., et al. 2011, A&A, 526, A49
Kann, D. A., Agayeva, S., Aivazyan, V., et al. 2023, arXiv:2302.06225
Kann, D. A., & Agui Fernandez, J. F. 2022, GCN, 32762, 1
Kozlova, A. V., Svinkin, D. S., Lysenko, A. L., et al. 2019, JPhCS, 1400, 022014
Kozyrev, A. S., Golovin, D. V., Litvak, M. L., et al. 2022, GCN, 32805, 1
Krimm, H. A., Barthelmy, S. D., Dichiara, S., et al. 2022, GCN, 32688, 1
Lapshov, I., Molkov, S., Mereminsky, I., et al. 2022, GCN, 32663, 1
Lesage, S., Veres, P., Briggs, M. S., et al. 2023, arXiv:2303.14172
Lesage, S., Veres, P., Roberts, O. J., et al. 2022, GCN, 32642, 1
Levin, V., Molkov, S., Mereminskiy, I., et al. 2021, GCN, 30283, 1
Lien, A., Sakamoto, T., Barthelmy, S. D., et al. 2016, ApJ, 829, 7
Liu, J. C., Zhang, Y. Q., Xiong, S. L., et al. 2022, GCN, 32751, 1
Lysenko, A. L., Anfinogentov, S. A., Svinkin, D. S., Frederiks, D. D., & Fleishman, G. D. 2019, ApJ, 877, 145
Lysenko, A. L., Ulanov, M. V., Kuznetsov, A. A., et al. 2022, ApJS, 262, 32
MacFadyen, A. I., & Woosley, S. E. 1999, ApJ, 524, 262
Malesani, D. B., Levan, A. J., Izzo, L., et al. 2023, arXiv:2302.07891
Mazets, E. P., Aptekar, R. L., Butterworth, P. S., et al. 1999a, ApJL, 519, L151
Mazets, E. P., Cline, T. L., Aptekar', R. L., et al. 1999b, AstL, 25, 635
Mazets, E. P., Golenetskii, S. V., Ilinskii, V. N., et al. 1981, Ap&SS, 80, 3
Mészáros, P., & Rees, M. J. 1997, ApJ, 476, 232
Metzger, B. D., Giannios, D., Thompson, T. A., Bucciantini, N., & Quataert, E. 2011, MNRAS, 413, 2031
Mitchell, L. J., Phlips, B. F., & Johnson, W. N. 2022, GCN, 32746, 1
Negro, M., Di Lalla, N., Omodei, N., et al. 2023, ApJL, 946, L21
Nousek, J. A., Kouveliotou, C., Grupe, D., et al. 2006, ApJ, 642, 389
O'Connor, B., Troja, E., Ryan, G., et al. 2023, arXiv:2302.07906
Paczyński, B. 1998, ApJL, 494, L45
Pavlinsky, M., Tkachenko, A., Levin, V., et al. 2021, A&A, 650, A42
Piano, G., Verrecchia, F., Bulgarelli, A., et al. 2022, ATel, 15662, 1
Pillera, R., Bissaldi, E., Omodei, N., et al. 2022, GCN, 32658, 1
Planck Collaboration, Ade, P. A. R., Aghanim, N., et al. 2016, A&A, 594, A13
Planck Collaboration, Aghanim, N., Akrami, Y., et al. 2020, A&A, 641, A6
Racusin, J. L., Liang, E. W., Burrows, D. N., et al. 2009, ApJ, 698, 43
Ravasio, M. E., Sharan Salafia, O., Oganesyan, G., et al. 2023, arXiv:2303.16223
Ripa, J., Pal, A., Werner, N., et al. 2022, GCN, 32685, 1
Sari, R., Piran, T., & Halpern, J. P. 1999, ApJL, 519, L17
Sunyaev, R., Arefiev, V., Babyshkin, V., et al. 2021, A&A, 656, A132
Svinkin, D., Frederiks, D., Ridnaia, A., et al. 2022, GCN, 32641, 1
Svinkin, D., Golenetskii, S., Frederiks, D., et al. 2021, GCN, 30276, 1
Svinkin, D. S., Frederiks, D. D., Aptekar, R. L., et al. 2016, ApJS, 224, 10
Tan, W. J., Li, C. K., Ge, M. Y., et al. 2022, ATel, 15660, 1
Tsvetkova, A., Frederiks, D., Golenetskii, S., et al. 2017, ApJ, 850, 161
Tsvetkova, A., Frederiks, D., Svinkin, D., et al. 2021, ApJ, 908, 83
Tsvetkova, A., Svinkin, D., Karpov, S., & Frederiks, D. 2022, Univ, 8, 373
Ursi, A., Panebianco, G., Pittori, C., et al. 2022, GCN, 32650, 1
van Putten, M. H. P. M., & Della Valle, M. 2017, MNRAS, 464, 3219
Veres, P., Burns, E., Bissaldi, E., et al. 2022, GCN, 32636, 1
Williams, M. A., Kennea, J. A., Dichiara, S., et al. 2023, ApJL, 946, L24
Xiao, H., Krucker, S., & Daniel, R. 2022, GCN, 32661, 1
Yonetoku, D., Murakami, T., Nakamura, T., et al. 2004, ApJ, 609, 935
Zhang, B., Fan, Y. Z., Dyks, J., et al. 2006, ApJ, 642, 354
Zhang, B., Zhang, B.-B., Virgili, F. J., et al. 2009, ApJ, 703, 1696